AAAS
Energy Material Advances
Volume 2021, Article ID 1959321, 10 pages
https://doi.org/10.34133/2021/1959321

Energy Material Advances
A SCIENCE PARTNER JOURNAL

Research Article

Intrinsic and Extrinsic Exciton Recombination Pathways in $AgInS_2$ Colloidal Nanocrystals

Matteo L. Zaffalon,[1] **Valerio Pinchetti**,[1] **Andrea Camellini**,[2] **Sergey Vikulov**,[3] **Chiara Capitani**,[1,4] **Bing Bai**,[5] **Meng Xu**,[5] **Francesco Meinardi**,[1] **Jiatao Zhang**,[5] **Liberato Manna**,[3] **Margherita Zavelani-Rossi**,[2,6] **Scott A. Crooker**,[7] **and Sergio Brovelli**[1]

[1]*Dipartimento di Scienza dei Materiali, Università degli studi di Milano-Bicocca, via Roberto Cozzi 55, 20125 Milano, Italy*
[2]*Dipartimento di Energia, Politecnico di Milano, Via Ponzio 34/3, 20133 Milano, Italy*
[3]*Istituto Italiano di Tecnologia, Via Morego 30, 16163 Genova, Italy*
[4]*Glass to Power SpA, Via Fortunato Zeni 8, 38068 Rovereto, Italy*
[5]*Beijing Key Laboratory of Construction-Tailorable Advanced Functional Materials and Green Applications, School of Materials Science & Engineering, Beijing Institute of Technology, Beijing 100081, China*
[6]*IFN-CNR, Piazza Leonardo da Vinci 32, 20133 Milano, Italy*
[7]*National High Magnetic Field Laboratory, Los Alamos National Laboratory, Los Alamos, New Mexico 87545, USA*

Correspondence should be addressed to Sergio Brovelli; sergio.brovelli@unimib.it

Received 11 January 2021; Accepted 24 February 2021; Published 5 April 2021

Ternary I-III-VI_2 nanocrystals (NCs), such as $AgInS_2$ and $CuInS_2$, are garnering interest as heavy-metal-free materials for photovoltaics, luminescent solar concentrators, LEDs, and bioimaging. The origin of the emission and absorption properties in this class of NCs is still a subject of debate. Recent theoretical and experimental studies revealed that the characteristic Stokes-shifted and long-lived luminescence of stoichiometric $CuInS_2$ NCs arises from the detailed structure of the valence band featuring two sublevels with different parity. The same valence band substructure is predicted to occur in $AgInS_2$ NCs, yet no experimental confirmation is available to date. Here, we use complementary spectroscopic, spectro-electrochemical, and magneto-optical investigations as a function of temperature to investigate the band structure and the excitonic recombination mechanisms in stoichiometric $AgInS_2$ NCs. Transient transmission measurements reveal the signatures of two subbands with opposite parity, and photoluminescence studies at cryogenic temperatures evidence a dark state emission due to enhanced exchange interaction, consistent with the behavior of stoichiometric $CuInS_2$ NCs. Lowering the temperature as well as applying reducing electrochemical potentials further suppress electron trapping, which represents the main nonradiative channel for exciton decay, leading to nearly 100% emission efficiency.

1. Introduction

Colloidal semiconductor nanocrystals (NCs) are a widely investigated class of solution-processable functional materials with growing potential in numerous optoelectronic and photonic technologies spanning from artificial lighting [1, 2] and lasers [3–6] to photovoltaics [7, 8], sensing [1, 9], and bioimaging [10, 11]. Among various NC compositions, ternary I-III-VI_2 NCs, such as $CuInS_2$ or $AgInS_2$ NCs, are rapidly emerging as nontoxic alternatives to conventional heavy-metal-based chalcogenides [12, 13] and can be synthetized in large quantities via high-throughput, noninjection techniques using inexpensive green precursors [14]. In addition to size-tunable electronic properties [15] and high luminescence quantum efficiency [14, 16, 17], I-III-VI_2 NCs exhibit distinctive optical properties including broadband optical absorption from the UV to the near-IR spectral regions, spectrally separated from a long-lived photoluminescence by a large Stokes shift which makes them promising candidates as optical markers for time-gated fluorescence bioimaging [18, 19] and as reabsorption-free emitters in photon management technologies such as large-area luminescent solar concentrators [2, 20–22]. Owing to their typically broad and featureless luminescence spectrum, $CuInS_2$ NCs have

also been proposed as active materials in single-component white LEDs [23, 24], enabling one to bypass the limitation of different turn-on voltages and degradation dynamics typically encountered in white-LEDs based on mixtures of NCs with complementary electroluminescence spectra [25, 26]. Because of their relevance for applications, numerous studies have been devoted to investigating the fundamental physical processes responsible for the distinctive optical and electronic behaviors of $CuInS_2$ NCs [7, 20, 27–30], as well as to identify and suppress competitive nonradiative processes affecting the luminescence yield [31]. Based on the strong similarities between the optical and magneto-optical behaviors of off-stoichiometry $CuInS_2$ NCs and Cu-doped II-VI chalcogenides [32–34], in such NCs, the large Stokes shift and long emission lifetime are typically ascribed to the recombination of a photogenerated conduction band (CB) electron with a photohole localized on an intragap defect state associated with Cu^+ defects [28, 35]. Alternatively, a self-trapped exciton model has been proposed where the highest occupied molecular orbital is due to the *3d* states of Cu^+ cations that localize the photohole also in the absence of lattice imperfections [32]. In stoichiometric, defect-free $CuInS_2$ NCs, on the other hand, the large Stokes shift and long-lived PL have been shown to originate from the detailed structure of the valence band (VB) featuring a high-energy hole sublevel with *even-parity* separated in energy from a lower-lying *odd-parity* sublevel [20, 36]. As a result of parity selection rules, the absorption edge in stoichiometric $CuInS_2$ NCs is dominated by the transition coupling the even-parity hole sublevel and the 1S electron level (which features s-type, and even-parity symmetry), while the long-lived and largely Stokes-shifted emission occurs via the partially allowed transition between the CB electron and the odd-parity sublevel where the photohole thermalizes.

Despite their comparably promising optical properties, $AgInS_2$ NCs have been much less investigated than $CuInS_2$ NCs [37–40]. Recently, building upon the theoretical description of the VB structure of $CuInS_2$ NCs by Efros and coworkers [36], Baimuratov et al. [41] theoretically investigated the origin of the optical behavior of $AgInS_2$ NCs also by taking into account the contribution of electron-phonon coupling and the additional effect of point defects. To date, however, detailed experimental studies of the photophysical mechanisms in $AgInS_2$ NCs have not yet been reported, and thus, our understanding of this important class of NCs lags behind that of their copper-based analogues.

In this work, we aim to contribute to this task by investigating the optical properties of $AgInS_2$ NCs using complementary spectroscopic techniques including continuous wave (*cw*) and time-resolved photoluminescence (PL), spectro-electrochemistry (SEC), ultrafast transient transmission (*TT*), and magnetic circular dichroism (MCD) experiments. Optical absorption and *TT* measurements enable us to resolve two spectral contributions responsible for the broadband absorption profile, while photoluminescence excitation (PLE) measurements reveal that the Stokes-shifted PL can also be excited using resonant excitation as much as 550 meV below the dominant absorption edge. This suggests that, similar to $CuInS_2$ NCs, the PL derives from an optical transition coupling the CB minimum to an *odd-parity* VB sublevel where the photohole thermalizes. *TT* dynamics enable us to quantify the hole localization time (1.4 ps), and temperature-dependent MCD measurements corroborate the absence of paramagnetic intragap states involved in the Stokes-shifted PL of ternary I-III-VI_2 chalcogenide NCs. In order to identify the main nonradiative pathways affecting the PL quantum efficiency of our NCs—in view of their application as active materials in optoelectronic devices—we perform spectro-electrochemistry measurements and PL experiments as a function of temperature. The PL behavior under applied electrochemical potential reveals that thermally assisted surface electron trapping is the main nonradiative loss channel, whose suppression via electrochemical passivation of electron traps or by lowering the sample temperature to 3.5 K leads to PL quantum efficiency close to unity. Interestingly, consistent with recent results on defect-free $CuInS_2$ NCs [20], the PL dynamics below $T \sim 50$ K show an almost 100-fold slowing down, at constant PL quantum yield (Φ_{PL}), thus pointing to a further fine structure of the emissive band-edge exciton state composed of the CB electron and the hole in the odd-parity VB sublevel. Crucially, side-by-side time-resolved PL measurements on Ag-doped CdSe NCs, where the photohole rapidly localizes on the Ag-dopant site, show exclusively the increase of the PL lifetime with decreasing temperature due to gradual suppression of thermally assisted nonradiative decay and no fine structure effects. This indirectly corroborates the picture that in ternary $AgInS_2$ NCs, the peculiar low-temperature PL kinetics are associated to the fine structure of the lowest excitonic level.

2. Materials and Methods

2.1. Materials. Silver(I) acetate (Ag(OAc), Puriss, ≥99.5%), indium(III) acetate ($In(OAc)_3$, 99.99%) and 1-dodecanethiol (DDT, ≥98%), sodium myristate (≥99%), selenium powder-100 mesh (99.99%), oleic acid, OA (≥90%), oleylamine, OLA (technical grade), thiourea (≥99%), cadmium nitrate tetrahydrate (≥98%), copper(II) chloride dihydrate (99.999%) 1-octadecene, ODE (≥90%), tributylphosphine, TBP (≥97%), tetrabutylammonium perchlorate, $TBAClO_4$ (for electrochemical analysis, ≥99.0%), and propylene carbonate, PC (anhydrous, ≥99.7%) were purchased from Sigma-Aldrich. Hexane (chromasolv, ≥97%), acetone (puriss, ≥99%), ethanol (puriss, ≥99%), and methanol (puriss, ≥99%) were purchased from Honeywell *Riedel-de-Haën*. All the chemicals were used without further purification.

2.1.1. Synthesis of $AgInS_2$ Nanocrystals. For the synthesis of $AgInS_2$ NCs was followed a heat-up procedure. A mixture of Ag(OAc) (0.2 mmol), $In(OAc)_3$ (0.2 mmol), thiourea (0.2 mmol) 3 mL OLA, and 2 mL of DDT was loaded into a three-neck flask and was degassed under vacuum at 110°C for 1 hour. Then, under nitrogen flow, the temperature was raised to 230°C for 15 minutes to let the particles grow. Finally, the reaction was quenched by cooling the solution to room temperature. The NCs were cleaned by precipitation with methanol and redispersion in hexane.

2.1.2. Synthesis of Ag:CdSe Nanocrystals. 3% Ag-doped CdSe NCs (~5 nm) started from Ag nanoparticles (NPs) as described by Liu et al. [42]. Monodisperse Ag NPs (~5 nm) were first prepared and reacted with a Se precursor in the molar ratio 1 : 5 at 50°C for the preparation of amorphous Ag_2Se NPs. The Se precursor was prepared from 1 mmol Se powder with 7 ml octadecylene at 270°C. The obtained Ag_2Se NCs (0.035 mmol) were dispersed in 10 ml toluene with 0.2 ml oleic acid (OA) and 0.1 ml oleylamine (OAm), then a 1 ml methanol solution containing 0.1 g $Cd(NO_3)_2{\cdot}4H_2O$ was added. After 2 min magnetic stirring, 0. ml tributylphosphine (TBP) was added, and the mixture was heated at 55°C for 1 h under magnetic stirring. The doping level was estimated by XPS analysis as described in ref. 34.

2.1.3. Inductively Coupled Plasma Atomic Emission Spectroscopy. ICP-AES analysis was performed by dissolving the NCs in HCl/HNO3 3 : 1 (*v*/*v*) and using an iCAP 6500 Thermo spectrometer.

2.1.4. Transmission Electron Microscopy. High-resolution TEM (HR-TEM) and high-angle annular dark field-scanning TEM (HAADF-STEM) imaging was performed on an image-C_S-corrected JEOL JEM-2200FS microscope (Schottky emitter), operated at an accelerating voltage of 200 kV.

2.1.5. Powder X-ray Diffraction. Powder XRD patterns were acquired in Bragg-Brentano geometry with Cu Kα radiation (Panalytical X'Pert Pro powder diffractometer).

2.1.6. Spectroscopic Studies. Absorption spectra of NCs in solution were measured with a Cary 50 UV-Vis spectrophotometer. Steady-state PL measurements were performed by exciting samples at 3.06 eV with ps-pulsed diode lasers (Picoquant LDH-P series, ~70 ps pulses). The emitted light was dispersed with a spectrometer and detected with a charge-coupled device. Photoluminescence quantum yield measurements were performed in an integrating sphere on NCs deposited onto silica substrates using the same excitation source and detection setup. The same films were mounted in the variable temperature insert of a closed cycle He cryostat for monitoring the dependence of the emission yield with temperature. Transient PL measurements at RT were carried out using the same excitation source at 3.06 eV from a pulsed diode laser. The emitted light was collected with a photomultiplier tube coupled to time-correlated single-photon counting unit (time resolution ~400 ps). Temperature-dependent PL and trPL measurements were carried out on NC thin films drop-casted on quartz substrates, excited using a frequency tripled pulsed Nd:YAG laser at 3.49 eV with a 150 Hz repetition rate (pulse duration, 5 ns), and mounted inside a cryostat with optical access.

2.1.7. Transient Transmission Spectroscopy. For the ultrafast transient transmission measurements, the laser source was a Ti:sapphire laser with chirped pulse amplification (Coherent LIBRA-HE), which provided 95 fs pulses at 800 nm at a repetition rate of 2 kHz. The excitation pulses at 1.97 and 2.3 eV were obtained by noncollinear optical parametric amplification in a beta-barium borate crystal. Pump pulse duration about 100 fs. The probe beam was a white light supercontinuum generated by focusing a small fraction of the fundamental beam onto a 2 mm thick sapphire plate. After chopping the pump beam at 1 kHz, pump and probe were focused on the sample by means of a lens and a spherical mirror. Pump fluence on the sample position was $\sim 11\,\mu J\ cm^{-2}$. A computer-controlled optical multichannel analyzer working at the repetition rate of the laser source acquires the map of the differential transmission $\Delta T/T = (T_{on} - T_{off})/T_{off}$, as a function of the pump-probe time delay; T_{on} and T_{off} are the probe spectra transmitted by the excited and unperturbed samples, respectively.

2.1.8. Spectro-Electrochemistry (SEC) Measurements. ITO-coated glass slides ($50 \times 7 \times 0.7$ mm, $R_S < 100\,\Omega$) were purchased from Delta Technologies (part no. CG-90IN-CUV). The ITO-coated surface was first covered with ZnO NPs (Nanograde, ~50 nm diameter) to avoid quenching of NC emission by fast charge/energy transfer to the ITO. The ZnO NP layer (~60 nm thick, measured using a Dektak profilometer) was deposited by dip-coating the glass/ITO substrate into an ethanol suspension of ZnO NPs ($2\ mg{\cdot}ml^{-1}$, one dip for 10 s) and annealed at 150°C for 10 min in a nitrogen glovebox. To test the stability of the glass/ITO/ZnO NP substrates during potential scans, we performed control experiments in which we monitored changes in optical absorption spectra for prolonged exposures to negative and positive potentials. The results of these measurements indicate that the substrates are unaffected by either positive or negative EC potentials for exposure times of tens of minutes, which are much longer than the measurement time used in our SEC experiments (~10 min). The NCs were deposited onto the ZnO NP layer as a few-monolayer-thick film by dip-coating from a dilute toluene solution. The ZnO NP layer used in this study was not treated with crosslinkers, and therefore, it represented a dielectric tunneling barrier of ~1 V. The introduction of the additional ZnO spacer as well as the presence of insulating surface ligands can also lead to an appreciable attenuation of the actual shift of the FL compared to the nominal applied EC potential. The ITO was connected as a working electrode to the potentiostat (Bio Logic SP-200 Research grade potentiostat/galvanostat), and the film was placed into a quartz cuvette filled with the electrolyte (0.1 M tetrabutylammonium perchlorate ($TBAClO_4$) in propylene carbonate). Ag and Pt wires were used as pseudoreference and counter electrodes, respectively. All potentials reported in this work were measured relative to the quasireference Ag electrode during staircase voltammetry scans (10 s per scan). The film was excited at 3.06 eV with a ps-pulsed-wave diode laser, and the emitted light was collected with a focusing lens and detected with a charge-coupled device spectrometer.

2.1.9. MCD Measurements. MCD measures the normalized difference in transmission between left- and right-circularly polarized light through films of nanocrystals in the Faraday geometry [43]. Nanocrystal films were mounted in the variable-temperature insert (1.5–300 K) of a 7 T superconducting magnet with direct optical access. Probe light of

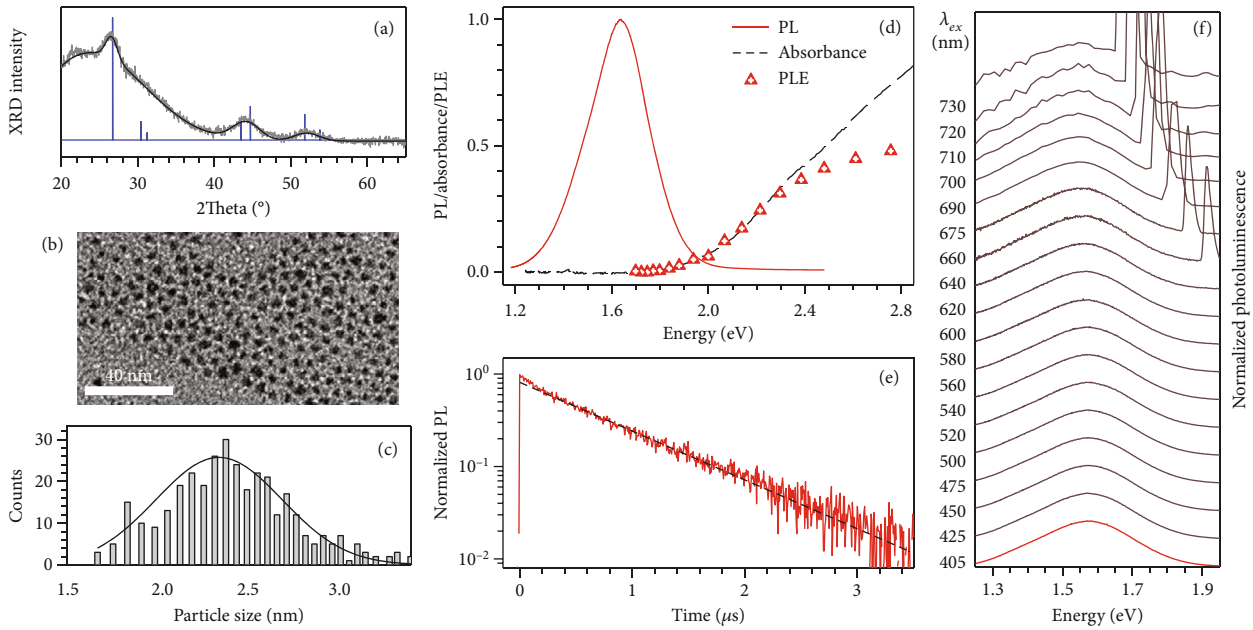

FIGURE 1: (a) X-ray diffraction pattern of $AgInS_2$ NCs at room temperature. The blue line corresponds to the XRD pattern for tetragonal $AgInS_2$ (PDF Card 03-065-5163). (b) TEM overview image of $AgInS_2$ NC sample featuring mean radius. (c) $AgInS_2$ NC size distribution extracted from (b). (d) Optical absorption (black dashed line), PL (solid red line, excitation at 3.06 eV), and PLE (triangles) spectra for a colloidal NC solution in toluene. (e) Normalized PL decay measured at 1.64 eV. (f) PL spectra of the same NCs under progressively lower energy excitation (from the bottom to top corresponding to the PLE data in panel 'b').

tunable wavelength was derived from a Xenon lamp directed through a spectrometer. The probe light was mechanically chopped at 137 Hz and was modulated between right and left circular polarizations at 50 kHz using a photoelastic modulator. The transmitted light was detected with a silicon avalanche photodiode.

3. Results

$AgInS_2$ NCs were synthesized following the heat-up method proposed by Torimoto and coworkers [16] using a metal acetate precursor ratio of 1 : 1 In : Cu and thiourea in a mixture of oleylamine and 1-dodecanthiol solution. Using such a precursor ratio, we obtained stoichiometric $AgInS_2$ NCs with In : Ag : S ratios of to 1.06 : 1 : 2.04, as confirmed by elemental analysis by inductively coupled plasma atomic emission spectroscopy (ICP-AES). The obtained NCs were of tetragonal crystal structure with radius distribution of 2.3 ± 0.4 nm (Figures 1(a)–1(c)). The optical absorption spectrum of the NCs in toluene (Figure 1(d)) shows the characteristic broadband profile of I-III-VI_2 NCs with an absorption shoulder at ~2.25 eV and a low-energy tail extending into the PL peak. The broad (FWHM ~0.3 eV) PL spectrum is centered at 1.64 eV corresponding to a Stokes shift as large as ~650 meV from the absorption shoulder. The Φ_{PL} at room temperature is 40 ± 5%. Consistent with previous reports [38], the corresponding PL dynamics (Figure 1(e)) are nearly single-exponential—except for a slightly faster initial drop possibly due to charge trapping—with lifetime $\tau = 820$ ns (as extracted from single exponential fitting of the dominant PL decay excluding the initial fast drop). Interestingly, the PLE spectrum collected at the PL maximum resembles nearly perfectly the low-energy absorption tail, and the respective PL spectra excited at progressively lower energy (Figure 1(f)) show no significant difference in shape or energy position with respect to each other or in comparison with the PL spectrum excited well above the absorption shoulder at 3.1 eV. The constant PL linewidth suggests that the exciton thermalizes to the same state below the dominant absorption shoulder, independently from the excitation energy.

More detailed insights into the structure of the absorption spectrum and the carrier dynamics are obtained by ultrafast *TT* spectroscopy using a spectrally selective pump operating in the low-fluence regime (when the number of photons absorbed per NC per pulse is much less than unity). Upon pumping above the absorption shoulder at 2.3 eV (Figure 2(a)), the differential transmittance ($\Delta T/T$) spectrum exhibits two intense bleaching bands at ~2.25 eV and ~2.05 eV (indicated as "A" and "B") in good correspondence with the absorption shoulder and with the low-energy tail of the steady-state absorption profile, respectively. The inspection of *TT* dynamics in Figure 2(b) shows an almost instantaneous photobleaching of the A transition—comparable with the temporal resolution of the experimental setup (~100 fs)—while the B signal grows more slowly with a rise time of 1.4 ps. These results support the VB structure model with the A band corresponding to the parity-allowed optical transition coupling the even-parity VB sublevel and the CB minimum, which also features an even-parity symmetry. On the other hand, the B band is associated with a lower-energy transition coupling the odd-parity VB sublevel and

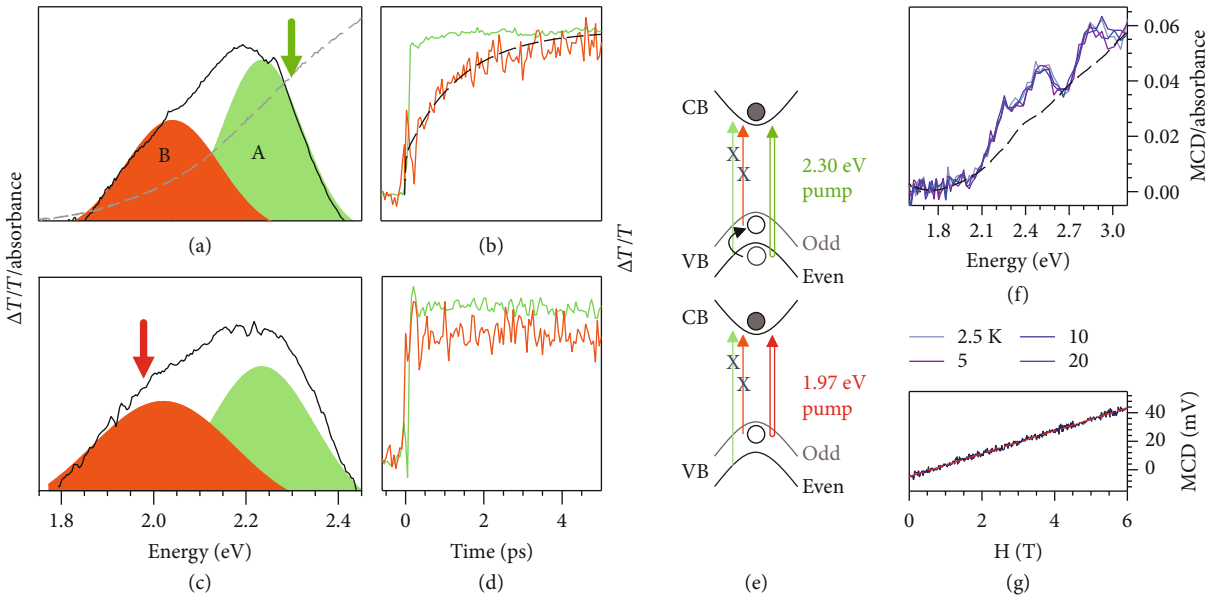

FIGURE 2: (a) Normalized transient transmission spectrum of $AgInS_2$ NCs collected at 5 ps after pumping at 2.3 eV in low fluence regime highlighting the A and B transitions, depicted here as shaded areas. Steady-state absorption spectrum for the same toluene solution of NCs used in *TT* measurements is reported as grey dashed line. The short green arrow shows the pumping energy. (b) Normalized bleaching $\Delta T/T$ kinetics for the A transition at 2.25 eV (green line) and for the B band at 1.9 eV (red line) after pumping close to the band-edge at 2.3 eV to avoid thermalization effects. The dashed line is a fit to an exponential rise function with 1.4 ps characteristic time. (c, d) Same as (a) and (b), but for pumping within the B transition band at 1.97 eV. A short red arrow shows the pumping energy. (e) Schematic diagram of the photophysical mechanism occurring at different pumping energies: slightly above the absorption shoulder at 2.3 eV (top panel) and within the B transition at 1.97 eV (bottom panel). Crossed thin vertical lines emphasize transition bleaching after the pump event. (f) MCD spectra at 6 T, at different temperatures (T = 2.5, 5, 10, 20 K). The dashed line is the absorption spectrum for the polymeric slab containing $AgInS_2$ NCs used in MCD measurements. (g) MCD signal collected at 2.5 K showing linear trend with the magnetic field.

the CB. This transition exhibits small oscillator strength due to the parity selection rules. The slow photobleaching rise-time observed for the B signal (Figure 2(b)) is related to hole dynamics; in particular, pumping above the absorption shoulder, it describes thermalization of the photohole from the higher-lying even-parity hole sublevel to the odd-parity sublevel. Following this picture, pumping directly within the B bleaching band should not change the *TT* spectrum since promoting electrons from the odd states into the CB inhibits also the A band transition. Furthermore, direct excitation of odd VB sublevel would result in an instantaneous bleaching also for the B signal. To explore this scenario, we selectively pump at 1.97 eV, far below the absorption shoulder. The resulting $\Delta T/T$ spectrum is nearly unchanged showing both A and B bands (Figure 2(c)), while bleaching dynamics are now also instantaneous for the B signal (Figure 2(d)). As a result, the overall *TT* analysis corroborates the VB structure model showing two transitions separated in energy by ~0.2 eV that we ascribe to odd- and even-parity VB sublevels, and reveals an efficient photohole thermalization process occurring at the picosecond timescale.

We point out that similar *TT* dynamics have been observed [34] for Ag:CdSe NCs where silver atoms undergo a transient photooxidation from the nonmagnetic Ag^+ ($[Kr]4d^{10}$) configuration to Ag^{2+} ($[Kr]4d^9$) which behaves as a paramagnetic radiative acceptor centre for a CB electron. Crucially, the unpaired spin of the lone electron in the d-shell of Ag^{2+} couples strongly with the band-edge exciton, resulting in the characteristic nonlinear temperature and magnetic field MCD dependence due to *sp-d* exchange interactions [44]. Therefore, magneto-optical experiments can be used to corroborate the absence (or reveal the presence) of intra-gap metastable Ag^{2+}-like acceptor states also in our $AgInS_2$ NCs. In Figure 2(f), we report the MCD spectra at increasing temperature from 2.5 K to 20 K at constant magnetic field (H = 6 T). Importantly, opposite to what observed in Ag:CdSe NCs, the magnetic response of our stoichiometric $AgInS_2$ NCs is temperature independent, same as what found in stoichiometric $CuInS_2$ NCs [20]. Consistently, the MCD intensity at 2.5 K follows a linear trend with H, thus confirming the absence of *sp-d* exchange interaction between the semiconductor bands and Ag^{2+} lone spins. Therefore, our experimental results support a scenario in which the broad absorption profile is dominated by parity selection rules, while the long-lived PL arises from the parity-forbidden recombination of the $1S_e$ electron into the odd-parity VB state activated by photohole localization. Within this framework, and in accordance with theoretical predictions [41], strong electron-phonon coupling could be responsible for the homogenously broadened PL spectrum shape in $AgInS_2$ NCs [45], as previously reported in single-particle PL measurements [46–48] (FWHM ~0.2-0.35 eV). Consistent with [41], electron-phonon coupling also accounts for the additional ~450 meV spectral separation between absorption

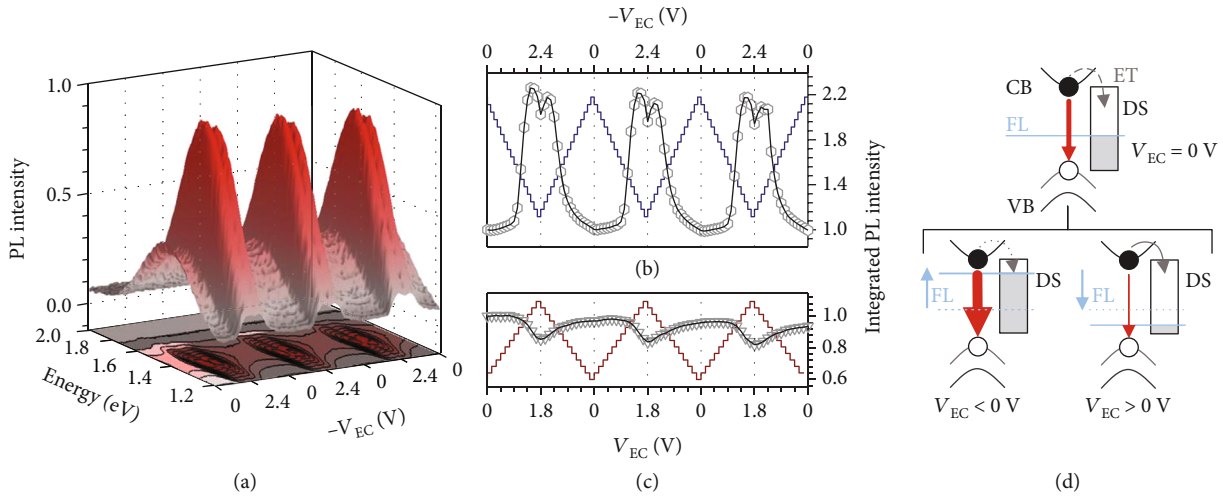

FIGURE 3: (a) Normalized PL spectra for $AgInS_2$ NCs at room temperature obtained during three cycles of staircase voltammetry with negative electrochemical potential (V_{EC}): lowered from 0 to -2.4 V and then back to 0 V (150 mV steps, each lasting 10 s). (b) Spectrally integrated and normalized PL intensity as a function of extracted from (a). The applied is reported in background as blue vertical step line. (c) Same as (b) for positive potential increasing from 0 to +1.8 V and then back to 0 V. (d) Schematic of the radiative recombination pathway (red arrow) and the competing nonradiative electron trapping processes (ET) to defect states (DS) shown as grey arrows. The effect of V_{EC} on PL intensity depends on the filling/emptying of DS (right of the band diagram) in response to changes in the position of the Fermi Level (FL) represented as a blue line.

shoulder and PL peak, leading, together to the ~200 meV separation due to the odd-even-parity VB effect to the observed ~650 meV Stokes shift.

With a view to optimize these NCs for optoelectronic applications, we conducted SEC experiments to obtain a picture of the principal loss channels. Electrochemical measurements are performed as cyclic staircase voltammetry for negative and positive electrochemical potentials (V_{EC}) against a silver-wire pseudoreference electrode. These measurements can be interpreted in terms of a deliberate modulation of the Fermi level (FL) where negative (positive) V_{EC} is equivalent to raising (lowering) the FL, resulting in a reversible passivation (activation) of surface electron traps associated with undercoordinated surface atoms or dangling bonds [31]. In Figure 3(a), we show the complete set of PL spectra for $AgInS_2$ NCs under application of negative V_{EC} cyclically scanned between 0 and -2.4 V. Notably, the PL maximum exhibits a 0.18 eV red-shift after drop-casting on indium tin oxide (ITO)/ZnO substrate, ascribable to energy transfer processes in aggregated NC films as previously reported in core-shell $CuInS_2$/ZnS NCs [49]. To quantify the effect of raising the FL on the PL intensity, we plot the integrated PL intensity as a function of the applied potential (Figure 3(b)), showing almost no effects at the initial stage of the potential ramp (up to $V_{EC} = -1.2$ V). This effect is common in SEC experiments using ITO/ZnO substrates, where the ZnO layer represents a dielectric tunnelling barrier resulting in a voltage drop across it [9]. By lowering the working electrode potential, the PL intensity undergoes a sudden growth by ~120% at -2.25 V. At even more negative potentials, the PL exhibits a reversible intensity drop likely associated with direct electron injection in the CB resulting in the activation of nonradiative Auger recombination [31, 43]. The PL evolution has been monitored during several cycles showing good reproducibility and symmetry by lowering and raising the applied potential, thus indicating that the voltage sweep does not damages the NC surfaces and that the passivation and activation of surface traps occur with similar time kinetics. On the other hand, by lowering the FL (Figure 3(c)), we observe a slight PL dimming (~15%) at 1.8 V that almost completely recovers when returning to $V_{EC} = 0$ V. The overall SEC behaviour—illustrated in Figure 3(d)—suggests that surface electron trapping (ET) is the dominant loss channel with respect to competitive surface hole trapping, and that its suppression would ultimately lead to Φ_{PL} close to unity. Similar suppression of electron trapping can be achieved growing a large bandgap shell; however, the use of zinc chalcogenides is typically accompanied by Zn diffusion into the NC core which modifies the electronic structure of the material. Hence, a defect-mediated radiative recombination is commonly invoked in alloyed $AgInS_2$/ZnS NCs to model their optical behaviour, where the defect's nature and position within the NC volume determine the PL energy and decay rate [50].

Complementary indications about loss channels in $AgInS_2$ NCs come from temperature-dependent steady state and time-resolved PL experiments. In Figure 4(a), we report a set of representative PL spectra at different temperatures in the range from $T = 300$ K to $T = 3.5$ K for $AgInS_2$ NCs showing monotonic growth of the PL intensity with decreasing T, saturating at $\Phi_{PL} \sim 100\%$ below 50 K (Figure 4(b)) and followed by a slight drop possibly due to nonradiative competitive channels which become competitive with the dark-exciton emission at low T. Nearly 100% PL efficiency indicates essentially complete suppression of thermally activated nonemissive channels and that the system has reached its

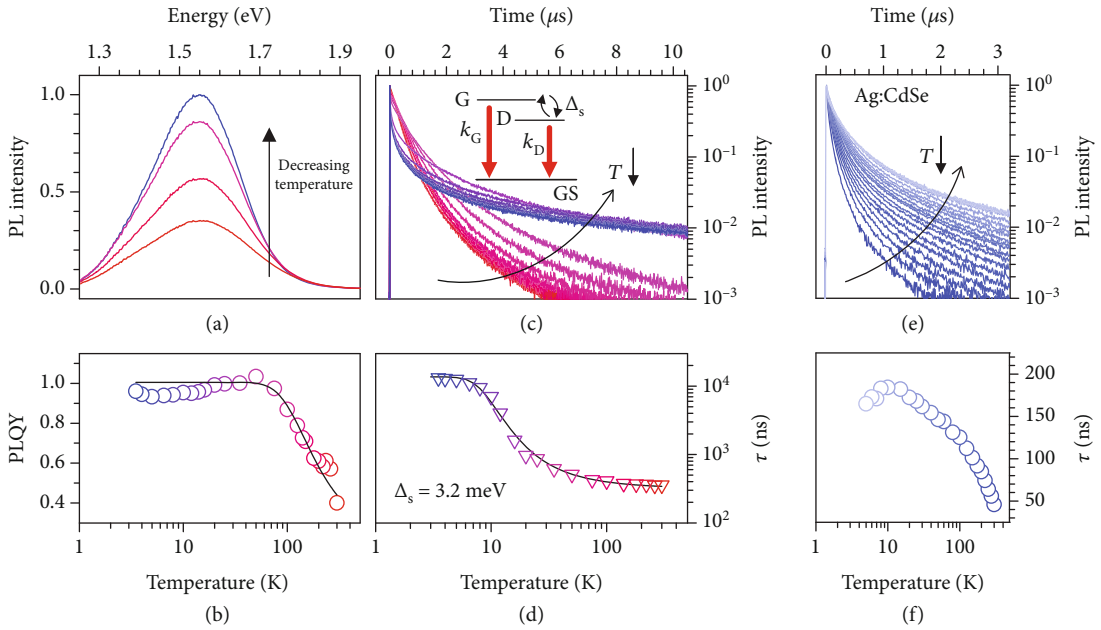

FIGURE 4: (a) Representative set of PL spectra of $AgInS_2$ NCs under pulsed laser excitation at 3.5 eV (355 nm) with 150 Hz repetition rate progressively lowering temperature from 300 K to 3.5 K (from red to blue: 300, 200, 100, 3.5 K). (b) Spectrally integrated and normalized PL intensity from (a) and corresponding Φ_{PL}. The solid black line represents the fit with the equation described in the text ($R^2 = 0.989$). (c) Decay curves for PL maximum at decreasing temperature from 300 to 3.5 K under 3.5 eV (355 nm) excitation at 150 Hz repetition rate. Inset: three-level model of grey (G) and dark (D) exciton states separated in energy by Δ_S. (d) PL decay lifetimes extracted from (c) as a function of temperature together with the respective fit (black line) to Equation (1). (e) PL decay curves for Ag:CdSe NCs at decreasing temperature from 300 K to 4 K (from blue to grey) collected at Ag-related PL maximum (1.69 eV) under pulsed laser excitation at 3.5 eV (355 nm) with 500 Hz repetition rate. (f) PL decay lifetimes extracted from (e) as a function of temperature.

radiative regime. The relative Φ_{PL} increase at cryogenic temperatures is consistent with SEC experiments at negative potentials, suggesting that electron trapping at the NC surface is phonon-assisted.

By fitting the integrated PL intensity evolution with T to the function [45, 51] $I_{PL}(T) = c/(1 + q * \exp(-E_a/k_B T))$ where c is a scaling factor, k_B is the Boltzmann constant, and q is a fitting parameter acting as a weight for the probability of this process, we obtain the trapping activation energy $E_a \sim 29$ meV, similarly to previous reports [20]. To further investigate temperature-assisted losses, we perform time-resolved PL measurements, as a function of T, showing gradual lengthening of the PL dynamics with decreasing T (Figure 4(c)). We notice that for $T > 50$ K, the zero-delay PL intensifies with no significant variation of τ by cooling down the system before reaching Φ_{PL} maximum at 50 K: this behaviour is largely due to suppression of ultrafast charge trapping channels depleting the NC bands faster than our temporal resolution. Strikingly, by lowering the temperature below 50 K, PL kinetics slows down dramatically and becomes double-exponential with an initial fast portion followed by a tens-of-microseconds long component, nearly two orders of magnitude slower than kinetics at 300 K (Figure 4(d)). This behaviour occurring at constant Φ_{PL} is in very good agreement with previous observations for stoichiometric $CuInS_2$ NCs [20] and suggests a further fine structure of the band edge exciton featuring a higher lying emissive state and a nonemissive state in thermal equilibrium with the environment and responsible for the long PL decay at low T. In analogy to stoichiometric $CuInS_2$ NCs, both such states belong to the weakly allowed exciton consisting of a CB electron and a hole in the odd-parity VB sublevel. Therefore, we label the long-lived weakly emissive exciton as "dark" (D) and the higher-lying emissive exciton as "grey" (G), to distinguish the current case from the case of CdSe quantum dots, where the emissive state is optically allowed and therefore referred to as "bright." By assuming a Boltzmann distribution of excitons between these two dark and grey states, we model the transition between the slow and fast decay regimes with a three-level scheme (inset of Figure 4(c)), by expressing the radiative decay rate as

$$k_{RAD}(T) = \tau_{RAD}^{-1}(T) = \left(k_D + k_G e^{-\Delta_s/k_B T}\right)\left(1 + e^{-\Delta_s/k_B T}\right)^{-1}, \quad (1)$$

where k_D and k_G are the radiative decay rates of dark and grey excitonic states, respectively, k_B is the Boltzmann constant, and Δ_S being the respective splitting energy. The model yields a Δ_S value of 3.2 meV consistent with what found in $CuInS_2$ NCs of similar size [20]. Importantly, analogous temperature-controlled time-resolved PL measurements on Ag:CdSe NCs (Figures 4(e) and 4(f)) show exclusively the lengthening of PL decays with decreasing T due to suppression of thermally activated nonradiative channels and no fine structure effects, thus corroborating the picture that the observed optical behaviour is direct consequence of the band edge exciton structure of $AgInS_2$ NCs and not to the involvement of localized defect states.

4. Discussion

In summary, we combined ultrafast *TT* and MCD spectroscopies as well as temperature-dependent PL and SEC experiments to investigate the recombination mechanisms in ternary $AgInS_2$ NCs. Optical absorption and *TT* measurements reveal two spectral contributions responsible for the broadband absorption profile, in agreement with recent theoretical models. Temperature-dependent MCD experiments indicate the absence of Ag-related intragap acceptor states acting as radiative recombination centers. Time-resolved PL measurements as a function of temperature show a further fine structure of the band-edge exciton that is not present in Ag:CdSe NCs, which we associate with the intrinsic (not trap-mediated) PL nature in $AgInS_2$ NCs. Finally, temperature-dependent PL and SEC experiments reveal that surface electron trapping is the main nonradiative loss channel that can be suppressed via electrochemical passivation of electron traps or by lowering the temperature to 3.5 K, leading to PL efficiency close to unity.

Data Availability

The data that support the findings of this study are available from the corresponding author upon reasonable request.

Conflicts of Interest

The authors declare no conflict of interest.

Acknowledgments

M.L.Z., C.C., V.P., and S.B. thank the MIUR "Dipartimenti di Eccellenza 2017 Project–Materials for Energy". Work at the NHMFL was supported by NSF DMR-1644779, the State of Florida, and the US DOE. A.C. and M.Z.-R. acknowledge the project MIUR-PRIN 2015 grant no. 2015WTW7J3 for financial support. C.C., and S.B. thank the Provincia Autonoma di Trento for financial support (Nanofarm Project). J. Z, B.B. and M. X. acknowledge support from the National Natural Science Foundation of China (Nos. 51872030 and 51631001).

References

[1] M. V. Kovalenko, L. Manna, A. Cabot et al., "Prospects of nanoscience with nanocrystals," *ACS Nano*, vol. 9, no. 2, pp. 1012–1057, 2015.

[2] J. M. Pietryga, Y. S. Park, J. Lim et al., "Spectroscopic and device aspects of nanocrystal quantum dots," *Chemical Reviews*, vol. 116, no. 18, pp. 10513–10622, 2016.

[3] J. Roh, Y. S. Park, J. Lim, and V. I. Klimov, "Optically pumped colloidal-quantum-dot lasing in LED-like devices with an integrated optical cavity," *Nature Communications*, vol. 11, no. 1, p. 271, 2020.

[4] M. Zavelani-Rossi, R. Krahne, G. Della Valle et al., "Self-assembled CdSe/CdS nanorod micro-lasers fabricated from solution by capillary jet deposition," *Laser & Photonics Reviews*, vol. 6, no. 5, pp. 678–683, 2012.

[5] Y.-S. Park, J. Roh, B. T. Diroll, R. D. Schaller, and V. I. Klimov, "Colloidal quantum dot lasers," *Nature Reviews Materials*, 2021.

[6] C. She, I. Fedin, D. S. Dolzhnikov et al., "Red, yellow, green, and blue amplified spontaneous emission and lasing using colloidal CdSe nanoplatelets," *ACS Nano*, vol. 9, no. 10, pp. 9475–9485, 2015.

[7] J. Du, R. Singh, I. Fedin, A. S. Fuhr, and V. I. Klimov, "Spectroscopic insights into high defect tolerance of Zn:$CuInSe_2$ quantum-dot-sensitized solar cells," *Nature Energy*, vol. 5, no. 5, pp. 409–417, 2020.

[8] D. H. Jara, S. J. Yoon, K. G. Stamplecoskie, and P. V. Kamat, "Size-dependent photovoltaic performance of $CuInS_2$ Quantum dot-sensitized solar cells," *Chemistry of Materials*, vol. 26, no. 24, pp. 7221–7228, 2014.

[9] M. Lorenzon, L. Sortino, Q. Akkerman et al., "Role of nonradiative defects and environmental oxygen on exciton recombination processes in $CsPbBr_3$ perovskite nanocrystals," *Nano Letters*, vol. 17, no. 6, pp. 3844–3853, 2017.

[10] A. L. Efros, J. B. Delehanty, A. L. Huston, I. L. Medintz, M. Barbic, and T. D. Harris, "Evaluating the potential of using quantum dots for monitoring electrical signals in neurons," *Nature Nanotechnology*, vol. 13, no. 4, pp. 278–288, 2018.

[11] G. Xu, S. Zeng, B. Zhang, M. T. Swihart, K. T. Yong, and P. N. Prasad, "New generation cadmium-free quantum dots for biophotonics and nanomedicine," *Chemical Reviews*, vol. 116, no. 19, pp. 12234–12327, 2016.

[12] P. Reiss, M. Carrière, C. Lincheneau, L. Vaure, and S. Tamang, "Synthesis of semiconductor nanocrystals, focusing on nontxoxic and earth-abundant materials," *Chemical Reviews*, vol. 116, no. 18, pp. 10731–10819, 2016.

[13] T. Torimoto, T. Kameyama, and S. Kuwabata, "Photofunctional materials fabricated with chalcopyrite-type semiconductor nanoparticles composed of $AgInS_2$ and its solid solutions," *The Journal of Physical Chemistry Letters*, vol. 5, no. 2, pp. 336–347, 2014.

[14] L. Li, A. Pandey, D. J. Werder, B. P. Khanal, J. M. Pietryga, and V. I. Klimov, "Efficient synthesis of highly luminescent copper indium sulfide-based core/shell nanocrystals with surprisingly long-lived emission," *Journal of the American Chemical Society*, vol. 133, no. 5, pp. 1176–1179, 2011.

[15] T. Torimoto, M. Tada, M. Dai, T. Kameyama, S. Suzuki, and S. Kuwabata, "Tunable photoelectrochemical properties of chalcopyrite $AgInS_2$ nanoparticles size-controlled with a photoetching technique," *Journal of Physical Chemistry C*, vol. 116, no. 41, pp. 21895–21902, 2012.

[16] T. Kameyama, T. Takahashi, T. Machida et al., "Controlling the electronic energy structure of ZnS–$AgInS_2$ solid solution nanocrystals for photoluminescence and photocatalytic hydrogen evolution," *Journal of Physical Chemistry C*, vol. 119, no. 44, pp. 24740–24749, 2015.

[17] Z. Bai, W. Ji, D. Han et al., "Hydroxyl-terminated $CuInS_2$ based quantum dots: toward efficient and bright light emitting diodes," *Chemistry of Materials*, vol. 28, no. 4, pp. 1085–1091, 2016.

[18] L. Li, T. J. Daou, I. Texier, T. T. Kim Chi, N. Q. Liem, and P. Reiss, "Highly luminescent $CuInS_2$/ZnS core/shell nanocrystals: cadmium-free quantum dots for in vivo imaging," *Chemistry of Materials*, vol. 21, no. 12, pp. 2422–2429, 2009.

[19] D. Aldakov, A. Lefrançois, and P. Reiss, "Ternary and quaternary metal chalcogenide nanocrystals: synthesis, properties

and applications," *Journal of Materials Chemistry C*, vol. 1, no. 24, p. 3756, 2013.

[20] A. Anand, M. L. Zaffalon, G. Gariano et al., "Evidence for the band-edge exciton of $CuInS_2$ Nanocrystals enables record efficient large-area luminescent solar concentrators," *Advanced Functional Materials*, vol. 30, no. 4, p. 1906629, 2020.

[21] F. Meinardi, H. McDaniel, F. Carulli et al., "Highly efficient large-area colourless luminescent solar concentrators using heavy-metal-free colloidal quantum dots," *Nature Nanotechnology*, vol. 10, no. 10, pp. 878–885, 2015.

[22] C. Li, W. Chen, D. Wu et al., "Large stokes shift and high efficiency luminescent solar concentrator incorporated with $CuInS_2$/ZnS quantum dots," *Scientific Reports*, vol. 5, no. 1, article 17777, 2016.

[23] D. Y. Jo, D. Kim, J. H. Kim et al., "Tunable white fluorescent copper gallium sulfide quantum dots enabled by Mn doping," *ACS Applied Materials and Interfaces*, vol. 8, no. 19, pp. 12291–12297, 2016.

[24] B. Chen, N. Pradhan, and H. Zhong, "From large-scale synthesis to lighting device applications of ternary I-III-VI semiconductor nanocrystals: inspiring greener material emitters," *Journal of Physical Chemistry Letters*, vol. 9, no. 2, pp. 435–445, 2018.

[25] S. Wepfer, J. Frohleiks, A. R. Hong, H. S. Jang, G. Bacher, and E. Nannen, "Solution-processed $CuInS_2$-based white QD-LEDs with mixed active layer architecture," *ACS Applied Materials and Interfaces*, vol. 9, no. 12, pp. 11224–11230, 2017.

[26] J. H. Kim, K. H. Lee, H. D. Kang et al., "Fabrication of a white electroluminescent device based on bilayered yellow and blue quantum dots," *Nanoscale*, vol. 7, no. 12, pp. 5363–5370, 2015.

[27] K. E. Knowles, K. H. Hartstein, T. B. Kilburn et al., "Luminescent colloidal semiconductor nanocrystals containing copper: synthesis, photophysics, and applications," *Chemical Reviews*, vol. 116, no. 18, pp. 10820–10851, 2016.

[28] H. D. Nelson and D. R. Gamelin, "Valence-band electronic structures of Cu^+-doped ZnS, alloyed Cu-In-Zn-S, and ternary $CuInS_2$ nanocrystals: a unified description of photoluminescence across compositions," *Journal of Physical Chemistry C*, vol. 122, no. 31, pp. 18124–18133, 2018.

[29] G. Nagamine, H. B. Nunciaroni, H. McDaniel, A. L. Efros, C. H. de Brito Cruz, and L. A. Padilha, "Evidence of band-edge hole levels inversion in spherical $CuInS_2$ quantum dots," *Nano Letters*, vol. 18, no. 10, pp. 6353–6359, 2018.

[30] H. J. Yun, J. Lim, J. Roh, D. C. J. Neo, M. Law, and V. I. Klimov, "Solution-processable integrated CMOS circuits based on colloidal $CuInSe_2$ quantum dots," *Nature Communications*, vol. 11, no. 1, p. 5280, 2020.

[31] V. Pinchetti, M. Lorenzon, H. McDaniel et al., "Spectroelectrochemical probing of intrinsic and extrinsic processes in exciton recombination in I-III-VI_2 nanocrystals," *Nano Letters*, vol. 17, no. 7, pp. 4508–4517, 2017.

[32] K. E. Knowles, H. D. Nelson, T. B. Kilburn, and D. R. Gamelin, "Singlet-triplet splittings in the luminescent excited states of colloidal Cu^+:CdSe, Cu^+:InP, and $CuInS_2$ nanocrystals: charge-transfer configurations and self-trapped excitons," *Journal of the American Chemical Society*, vol. 137, no. 40, pp. 13138–13147, 2015.

[33] K. E. Hughes, S. R. Ostheller, H. D. Nelson, and D. R. Gamelin, "Copper's role in the photoluminescence of $Ag_{1-x}Cu_xInS_2$ nanocrystals, from copper-doped $AgInS_2(x \sim 0)$ to $CuInS_2(x = 1)$," *Nano Letters*, vol. 19, no. 2, pp. 1318–1325, 2019.

[34] V. Pinchetti, Q. di, M. Lorenzon et al., "Excitonic pathway to photoinduced magnetism in colloidal nanocrystals with nonmagnetic dopants," *Nature Nanotechnology*, vol. 13, no. 2, pp. 145–151, 2017.

[35] A. Fuhr, H. J. Yun, N. S. Makarov, H. Li, H. McDaniel, and V. I. Klimov, "Light Emission Mechanisms in $CuInS_2$ Quantum dots evaluated by spectral electrochemistry," *ACS Photonics*, vol. 4, no. 10, pp. 2425–2435, 2017.

[36] A. Shabaev, M. J. Mehl, and A. L. Efros, "Energy band structure of $CuInS_2$ and optical spectra of $CuInS_2$ nanocrystals," *Physical Review B - Condensed Matter and Materials Physics*, vol. 92, no. 3, pp. 1–9, 2015.

[37] Y. Gromova, A. Sokolova, D. Kurshanov et al., "Investigation of $AgInS_2$/ZnS quantum dots by magnetic circular dichroism spectroscopy," *Materials*, vol. 12, no. 21, p. 3616, 2019.

[38] B. Mao, C. H. Chuang, J. Wang, and C. Burda, "Synthesis and photophysical properties of ternary I–III–VI $AgInS_2$ Nanocrystals: intrinsic versus surface states," *The Journal of Physical Chemistry C*, vol. 115, no. 18, pp. 8945–8954, 2011.

[39] S. O. M. Hinterding, M. J. J. Mangnus, P. T. Prins et al., "Unusual Spectral Diffusion of Single $CuInS_2$ Quantum Dots Sheds Light on the Mechanism of Radiative Decay," *Nano Letters*, vol. 21, no. 1, pp. 658–665, 2021.

[40] S. M. Harvey, D. W. Houck, M. S. Kirschner et al., "Transient Lattice Response upon Photoexcitation in $CuInSe_2$ Nanocrystals with Organic or Inorganic Surface Passivation," *ACS Nano*, vol. 14, no. 10, pp. 13548–13556, 2020.

[41] A. S. Baimuratov, I. Martynenko, A. V. Baranov, A. V. Fedorov, I. D. Rukhlenko, and S. Y. Kruchinin, "Giant stokes shifts in $AgInS_2$ Nanocrystals with trapped charge carriers," *Journal of Physical Chemistry C*, vol. 123, no. 26, pp. 16430–16438, 2019.

[42] J. Liu, Q. Zhao, J. L. Liu et al., "Heterovalent-doping-enabled efficient dopant luminescence and controllable electronic impurity via a new strategy of preparing II–VI nanocrystals," *Advanced Materials*, vol. 27, no. 17, pp. 2753–2761, 2015.

[43] C. Capitani, V. Pinchetti, G. Gariano et al., "Quantized electronic doping towards atomically controlled "charge-engineered" semiconductor nanocrystals," *Nano Letters*, vol. 19, no. 2, pp. 1307–1317, 2019.

[44] N. Samarth and J. K. Furdyna, "Diluted magnetic semiconductors," *MRS Bulletin*, vol. 13, no. 6, pp. 32–36, 1988.

[45] Y. Hamanaka, T. Ogawa, M. Tsuzuki, and T. Kuzuya, "Photoluminescence properties and its origin of $AgInS_2$ Quantum dots with chalcopyrite structure," *Journal of Physical Chemistry C*, vol. 115, no. 5, pp. 1786–1792, 2011.

[46] O. Stroyuk, F. Weigert, A. Raevskaya et al., "Inherently broadband photoluminescence in Ag–In–S/ZnS quantum dots observed in ensemble and single-particle studies," *The Journal of Physical Chemistry C*, vol. 123, no. 4, pp. 2632–2641, 2019.

[47] P. J. Whitham, A. Marchioro, K. E. Knowles, T. B. Kilburn, P. J. Reid, and D. R. Gamelin, "Single-particle photoluminescence spectra, blinking, and delayed luminescence of colloidal $CuInS_2$ nanocrystals," *Journal of Physical Chemistry C*, vol. 120, no. 30, pp. 17136–17142, 2016.

[48] D. K. Sharma, S. Hirata, L. Bujak et al., "Single-particle spectroscopy of I-III-VI semiconductor nanocrystals: spectral

diffusion and suppression of blinking by two-color excitation," *Nanoscale*, vol. 8, no. 28, pp. 13687–13694, 2016.

[49] S. Gardelis, M. Fakis, N. Droseros, D. Georgiadou, A. Travlos, and A. G. Nassiopoulou, "Energy transfer in aggregated $CuInS_2$/ZnS core-shell quantum dots deposited as solid films," *Journal of Physics D: Applied Physics*, vol. 50, no. 3, article 035107, 2017.

[50] Y. Hamanaka, K. Watanabe, and T. Kuzuya, "Luminescence enhancement mechanisms of $AgInS_2$/ZnS core/shell nanoparticles fabricated by suppressing quaternary alloying," *Journal of Luminescence*, vol. 217, p. 116794, 2020.

[51] V. Dzhagan, O. Selyshchev, O. Raievska et al., "Phonon spectra of strongly luminescent nonstoichiometric Ag-In-S, Cu-In-S, and Hg-In-S nanocrystals of small size," *Journal of Physical Chemistry C*, vol. 124, no. 28, pp. 15511–15522, 2020.